Threshold behavior of interaction potential for the system ^{7}Li + ^{64}Ni: Comparison with ^{6}Li + ^{64}Ni

Md. Moin Shaikh [a,*], Mili Das [b], Subinit Roy [a], M. Sinha [a], M.K. Pradhan [c], P. Basu [a], U. Datta [a], K. Ramachandran [d], A. Shrivastava [d]

[a] *Nuclear Physics Division, Saha Institute of Nuclear Physics, Kolkata 700 064, India*
[b] *Physics Department, Anandamohan College, Kolkata 700 009, India*
[c] *Physics Department, Belda College, Belda, Paschim Medinipur 721 424, West Bengal, India*
[d] *Nuclear Physics Division, Bhabha Atomic Research Centre, Mumbai 400 085, India*

Abstract

The elastic scattering angular distributions for the system ^{7}Li + ^{64}Ni were measured in the bombarding energy range of 12 MeV $\leq$ E$_{lab}$ $\leq$ 26.4 MeV. A phenomenological optical model analysis was performed for the measured data. The strengths of the fitted potential components at the surface were estimated to extract their variation with energy. Further analyses of the measured angular distributions were performed with a *hybrid* potential composed of a renormalized folded real and a phenomenological imaginary potential. Both the model potentials predict similar energy dependent behavior for the effective interaction potential around the barrier. Unlike the heavy targets, ^{7}Li + ^{64}Ni does not show a normal threshold behavior. It also does not clearly exhibit a behavior similar to ^{6}Li + ^{64}Ni. The real potential for ^{7}Li + ^{64}Ni does not exhibit any significant energy dependence and the imaginary potential strength remains almost independent of energy above the Coulomb barrier ($\sim$ 14 MeV). However, at energies below the barrier, a sudden drop in the imaginary potential strength is observed.
© 2016 Elsevier B.V. All rights reserved.

---

* Corresponding author.
 E-mail address: moin.shaikh@saha.ac.in (Md.M. Shaikh).

1. Introduction

Breakup of one of the colliding partners in heavy-ion collision influences the scattering or the reaction processes in a manner not observed in collisions of strongly bound nuclei. Manifestation of the coupling of relative motion to breakup or breakup like channels are varied. It depends upon the breakup threshold of the projectile, the structure of its continuum and also on the mass of the target nucleus. It has, therefore, been the subject of extensive investigations over the last few decade [1–11].

One of the most important features of breakup coupling is its effect on the behavior of interaction potential describing the elastic scattering of weakly bound projectiles at energies close to the Coulomb barrier. For weakly bound nuclei it has been shown that the coupling of elastic channel to the channels with excitations above the breakup threshold produces a repulsive real dynamical polarization potential (DPP) [12,13]. This is contrary to the attractive real dynamical polarization generated due to coupling of elastic channel with the bound excited states of the systems. The latter behavior is well known as normal threshold anomaly (TA) [14]. The repulsive nature of the DPP due to breakup coupling is, therefore, responsible for the disappearance of TA for the weakly bound projectiles.

The weakly bound stable Li-isotopes, ^{6}Li ($S_\alpha = 1.47$ MeV) and ^{7}Li ($S_\alpha = 2.47$ MeV), have widely been used to probe the influence of breakup on the near barrier energy behavior of the potential. Studies involving ^{6}Li nucleus, with a predominant two-body $\alpha + d$ cluster structure, show that normal threshold behavior does not appear for this projectile irrespective of whether it is incident on a heavy or a light target [3,4,6–8,15–18].

The projectile ^{7}Li, the other loosely bound stable Li-isotope, appears to behave differently with the changing mass of the target. With heavier targets, like ^{208}Pb [3], it was found that the interaction potential exhibits TA. It was argued that, unlike ^{6}Li, for ^{7}Li projectile the real dynamic polarization potential resulting from the coupling to the $\alpha + t$ continuum is less repulsive in the surface region [19] and the absorption process at low energies is dominated by fusion reaction. However, the behavior changes as the target mass is decreased. For instance, threshold anomaly of any kind, TA or breakup modified TA, was not observed for ^{7}Li + ^{144}Sm system [20]. Two different inferences were reached for ^{7}Li + ^{138}Ba system. While Maciel et al. [4] concluded from their phenomenological optical model potential analysis of ^{7}Li + ^{138}Ba elastic scattering that the system exhibits TA. A later analysis by Gomes et al. [21] with parameter free Sao Paolo potential indicated the absence of TA. The conflicting conclusions could be due to lack of sufficient data to extract the energy dependence of effective potential. Investigation of ^{7}Li + ^{116}Sn yielded a potential behavior that is independent of incident energy [22] corroborating the observation of Ref. [21] for ^{7}Li + ^{138}Ba. With the target mass decreasing further, for ^{7}Li + ^{80}Se [23] and for ^{7}Li + ^{59}Co [24], the observations indicate that the systems tend to show the TA. For still lighter systems like ^{27}Al, Figueira et al. [25] found that no threshold anomaly exists for ^{7}Li + ^{27}Al, but for ^{7}Li + ^{28}Si [6] no such conclusion could be reached.

Thus the threshold behavior of the effective potential describing the elastic scattering of ^{7}Li does not display a consistent evolution like ^{6}Li. The behavior of the effective potential for scattering of ^{6}Li is dominated by the breakup of the projectile whereas the same for ^{7}Li appears to undergo a distinct change as the target mass decreases.

We present in this paper our investigation of the energy variation of the components of effective potential describing the elastic scattering of ^{7}Li projectile from the target ^{64}Ni at energies around the Coulomb barrier. The motivation is to see how the energy dependence of the potential for ^{7}Li + ^{64}Ni unfolds near the barrier – whether the behavior complies with the observations

for the targets in this mass region or it shows an energy independent behavior like those for the targets ^{144}Sm, ^{138}Ba and ^{116}Sn. A comparison with the observed behavior of the potential for ^{6}Li scattering from the same target in almost the same energy domain will also be performed. The particular interest stems from the fact that the stripping channel (^{7}Li, ^{6}Li) has a Q-value of -1.152 MeV while the channel (^{6}Li, ^{5}Li) has a Q-value of $+0.434$ MeV with ^{64}Ni target. The details of the experiment have been given in Section 2. The method of analysis and the extraction of the energy dependence of surface strengths of the potential components are given in Section 3, which is followed by the section with the results and discussions. Finally we summarize our work in section 5.

2. Experimental details

The experiment was carried out at the Pelletron Linac facility in Mumbai, India. A self-supporting target of ^{64}Ni, prepared by electron beam evaporation from 99% enriched metallic powder, was used for the present experiment. The thickness of the target was estimated to be 376 µg/cm^2 using the α energy loss method. The target was bombarded with ^{7}Li beam from the pelletron at energies of 12, 14.3, 15, 16, 19.3 and 26.4 MeV. The beam current during the experiment was varied from 1 to 12 pnA. The outgoing particles were detected by four $E - \Delta E$ telescopes with conventional silicon surface barrier detectors placed on a rotatable arm at an angular separation of 10°. Two of the telescopes with 15 µm, 25 µm thick ΔE detectors and 500 µm, 3 mm thick E detectors were set to detect the scattered particles at forward angles. Two similar set of telescopes were placed at backward angles. The solid angles subtended by the telescopes at the target center were 0.097, 0.081, 0.186 and 0.144 msr, respectively. Two monitor detectors of thickness 2 mm and 3 mm fitted with special 1 mmϕ Tantalum collimators were mounted at $\pm15°$ about the beam axis at a distance of 40.7 cm from the target center. These two detectors were used to monitor the beam position and also for the purpose of normalization. The calibration runs were taken with a standard ^{209}Bi target after each energy change. Using the Rutherford scattering cross sections for ^{7}Li incident on ^{209}Bi at lower energies, the detector solid angles and the relative normalizations between the telescopes were determined. The statistical error in the data is less than 2% in the forward angles and a maximum of 30% in the backward angles. The data were recorded using the data acquisition system LAMPS [26].

A representative spectrum for ^{7}Li + ^{64}Ni scattering at incident energy of 26.4 MeV for an angle close to the quarter point angle of 46° is shown in Fig. 1. Overall energy resolution achieved in the present experiment is about 190–260 keV for the range of incident energies used. The inelastically scattered ^{7}Li* ($E^* = 478$ keV) could be separated from the elastically scattered ^{7}Li. At the lowest energy in the back-angle region, the FWHM of the elastic peak is further worsened. However, the inelastic contribution being very small compared to the elastic, the peaks of scattered ^{7}Li at lower energies comprised purely of elastic events.

3. Analysis

Optical model (OM) analysis was carried out using three different model potentials. Firstly, the angular distribution data of ^{7}Li + ^{64}Ni were analyzed with the phenomenological OM potentials. Parametric Woods–Saxon (W-S) forms were used for both the real and imaginary potential components of the OM potential. In one of the phenomenological model calculations, the geometry parameters of the potential components were varied with energy while in the other the same were kept fixed at suitable values for all the incident energies. Subsequently, the data were
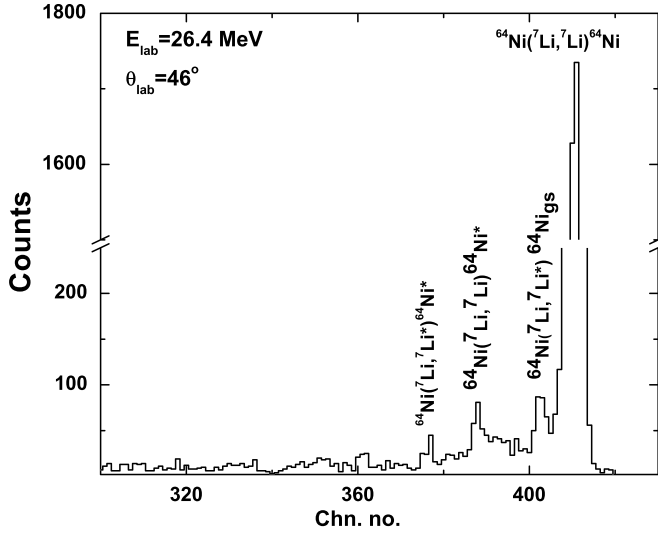
Fig. 1. Spectrum of ^{7}Li scattering from ^{64}Ni at incident energy of 26.4 MeV and laboratory angle of 46°.

further analyzed with a 'hybrid' potential consisting of renormalized folded real and parametric volume-type W-S imaginary components. The use of different model potentials was intended to make the extraction of the secondary data, the potential strengths at the radius of sensitivity as a function of energy, independent of the choice of model potential.

3.1. Phenomenological OM analysis

The phenomenological OM potential has the following form

$$U_{OM}(R) = V(R; V_o, R_o, a_o) + i[W_F(R; W_o, R_F, a_F) + W_D(R; W_s, R_s, a_s)] \tag{1}$$

where $V(R)$ denotes the volume type W-S real potential, $W_F(R)$ is a volume type W-S imaginary potential describing the core fusion part and $W_D(R)$ is a derivative type W-S imaginary potential to account for the absorption due to reactions occurring at the surface region. The parameters V_o, W_o and W_s are the strengths of the respective potentials with R's and a's denoting the radius and diffuseness parameters, respectively. The potential W_F with the parameters $W_o = 50.0$ MeV, $R_F = 1.0 \times (A_T^{1/3} + A_P^{1/3})$ fm and $a_F = 0.25$ fm simulates the ingoing wave boundary condition yielding the core fusion after the penetration of the barrier and was kept fixed for all the incident energies. The best fit parameters for ^{6}Li $+$ ^{64}Ni at 26 MeV from Ref. [15] were used as the starting parameters for ^{7}Li $+$ ^{64}Ni at 26.4 MeV. Search was performed over the parameters V_0, a_0, W_s and a_s, changing the real and surface imaginary radii in small steps using the code SFRESCO [27]. After optimizing the radius parameters at the highest energy, 26.4 MeV, the respective radii were kept fixed during the search for best fit parameters at lower bombarding energies. The search was then performed over the remaining parameters, *i.e.*, V_0, a_0, W_s and a_s, simultaneously at each incident energy using the 26.4 MeV parameters as the starting set. The best fit parameters, the minimum χ^2/N (N denotes the number of data points) values and the corresponding reaction cross sections σ_r are shown in Table 1. The errors associated with the reaction cross sections correspond to the limiting values of the reaction cross sections

Table 1
Best fit parameters with phenomenological potential for ^{7}Li + ^{64}Ni.

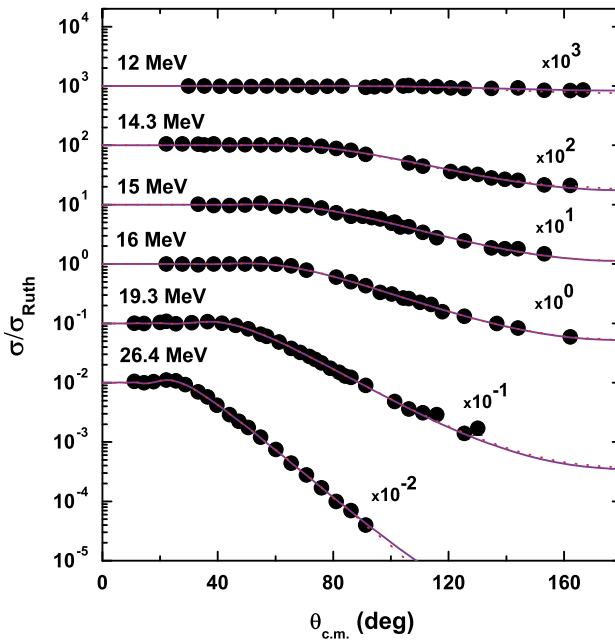| E_{lab} (MeV)	V_0 (MeV)	R_0 (fm)	a_0 (fm)	W_s (MeV)	R_s (fm)	a_s (fm)	χ^2/N	σ_r (mb)
12.0	39.34	6.0	0.801	0.86	7.4	0.931	0.12	$41.03^{+3.77}_{-2.33}$
14.3	47.12	6.0	0.782	1.99	7.4	0.907	0.86	$433.5^{+13.0}_{-3.70}$
15.0	40.20	6.0	0.763	2.20	7.4	0.894	1.36	$536.8^{+12.0}_{-23.6}$
16.0	43.84	6.0	0.743	2.10	7.4	0.884	0.89	$663.1^{+29.9}_{-20.5}$
19.3	48.77	6.0	0.742	2.24	7.4	0.868	1.03	$1060.2^{+80.7}_{-46.0}$
26.4	69.12	6.0	0.704	3.21	7.4	0.776	0.73	$1545.3^{+68.4}_{-37.5}$

Fig. 2. (Color online.) Elastic angular distributions of ^{7}Li + ^{64}Ni. The solid and dotted lines represent the predictions of phenomenological and hybrid model potentials respectively.

for the $\chi^2 = \chi^2_{min} + 1$ condition. The best fits model angular distributions are shown by solid lines in Fig. 2.

3.2. OM analysis with folded potential

The data were further analyzed using a *hybrid* model potential with the double-folded real potential, V_f generated from the density-dependent M3Y-Reid nucleon–nucleon interaction [28, 29] and a phenomenological volume type imaginary W-S potential

$$U_{OM}(R) = \lambda_r V_f(R) + i W_v(R; W_o, R_w, a_w). \tag{2}$$

Table 2
Best fit parameters with hybrid potential for ^{7}Li + ^{64}Ni.

E_{lab} (MeV)	λ_r	W_0 (MeV)	R_w (fm)	a_w (fm)	χ^2/N	σ_r (mb)
12.0	0.58	3.65	6.80	0.947	0.12	$40.9^{+3.4}_{-3.3}$
14.3	0.59	13.57	6.80	0.927	0.85	$442.6^{+20.3}_{-5.7}$
15.0	0.49	14.26	6.80	0.916	1.38	$538.3^{+14.6}_{-4.8}$
16.0	0.48	14.83	6.80	0.892	0.96	$665.3^{+20.7}_{-18.1}$
19.3	0.54	17.52	6.80	0.856	1.11	$1063.4^{+7.3}_{-28.7}$
26.4	0.55	20.64	6.80	0.830	0.94	$1559.9^{+87.5}_{-102.4}$

The density dependence of the interaction was included following the DDM3Y convention [30] as

$$F(\rho) = C[1 + \alpha \, exp(-\beta\rho)] \tag{3}$$

where $C = 0.2845$, $\alpha = 0.6391$ and $\beta = 2.9605$ fm^3. A linear energy dependent part of the form $g(E) = (1 - 0.002E)$ was incorporated to take into account the intrinsic energy dependence of the interaction [29]. The mass density distribution of ^{64}Ni was taken from Ref. [31]. The parametric form of ^{7}Li charge density was taken from Ref. [32]. The charge density is subsequently unfolded for finite proton distribution to get the point proton distribution. To obtain total density of ^{7}Li, it was assumed that both proton and neutron densities have same radial distribution. Hence, the total density for ^{7}Li was determined by normalizing the proton density distribution to A = 7.

In this model potential, the real part has a fixed geometry with only the renormalization factor λ_r to vary while the geometry of the imaginary part can be varied freely. The energy dependence of the imaginary radius, R_w, was assumed to be negligible and was kept fixed from the fit to the highest energy angular distribution data. Search was subsequently performed by varying the three parameters λ_r, W_o and a_w simultaneously. The best fit parameters along with the χ^2/N values and the reaction cross sections, σ_r, are given in Table 2. The normalizations, $\lambda_r \sim 0.5$ for real folded potential, obtained in the present case, are in contrast to the case of ^{7}Li + ^{208}Pb [3] but are similar to those found for ^{7}Li + ^{28}Si [6] and ^{7}Li + ^{138}Ba [6]. The errors associated with the reaction cross sections were estimated in the same way as described earlier. The predictions with the best fit hybrid model potential for ^{7}Li + ^{64}Ni are shown in Fig. 2 by dotted lines.

3.3. Radius of sensitivity and threshold behavior

To probe the real and imaginary potentials as functions of energy in the vicinity of the barrier, it is important to identify the radial region of sensitivity of the potentials, *i.e.*, the region where the potentials are best determined by the elastic scattering data. In order to find the radius of sensitivity, R_s, or the *crossing radius*, we adopted the procedure described in Ref. [33]. At each energy, a grid search on the diffuseness with a free search on the strength of the potential was performed, keeping the radius fixed. The procedure leads to a set of good potentials producing equivalent fits to the data at allowable χ^2 values. These 'good' potentials cross each other within a narrow radial region, indicating the R_s for the given set of data. The radius of sensitivity varies with incident energy. The mean radius of sensitivity (R_M) over the bombarding energy range
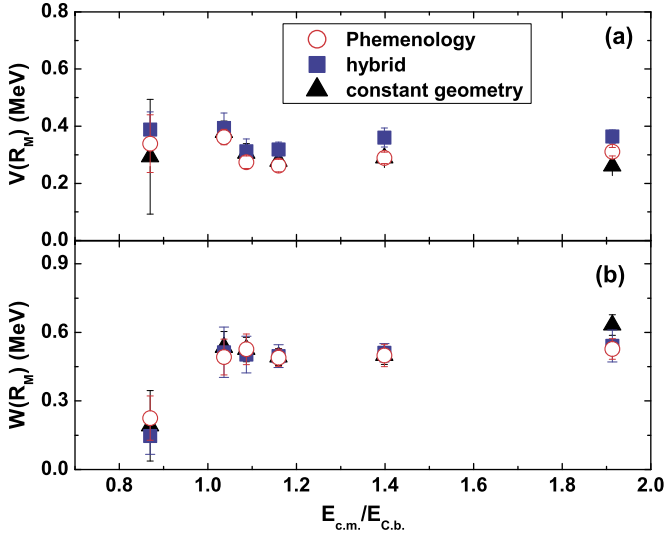
Fig. 3. (Color online.) Energy dependence of real and imaginary components of the effective potentials of ^{7}Li + ^{64}Ni. Open circle corresponds to phenomenological potential while solid squares represent the hybrid potential. Solid triangles in the figure depict the prediction of potential with geometries fixed. The potential values were determined at mean radius of sensitivity, $R_M = 9.8$ fm.

of the present study has the value 9.8 fm. The real and imaginary potentials at 9.8 fm from the phenomenological and the hybrid models for the system ^{7}Li + ^{64}Ni are shown in Fig. 3 as a function of $E_{c.m.}/E_{C.b.}$ where $E_{C.b.}$ (= 12.44 MeV) is the Coulomb barrier of the system. The error bars with each points in the figure include the distribution in the values of different good potentials and the uncertainty associated with the radius of sensitivity value. In the figure, the third plot corresponds to a phenomenological potential where the real and imaginary geometry parameters were independent of energy and only the strengths were varied to obtain the best fit at each energy. The radius and diffuseness of real and imaginary components of the best fit potential for 19.3 MeV incident energy were used for the fixed geometry potential. Three different model potentials, *viz*, the phenomenological potential with energy dependent geometry for real and imaginary components, hybrid potential with fixed geometry real and variable geometry imaginary and the fixed geometry real and imaginary phenomenological potentials, fitting the angular distributions produce very similar dependence on energy at the region of interest.

A closer look at Fig. 3 shows that the imaginary component decreases below the barrier but above the barrier the imaginary strengths at different incident energies are almost constant. Even the absorption remains high close to the barrier energy. On the other hand, over the measured energy values, the real potential strength V(R_M) remains constant within the error bar but exhibits a tendency to increase at the barrier energy.

As R_s is found to be energy dependent and a degree of uncertainty is associated with its value at each energy, we employed the method described by Brandan et al. [34] to look for the dispersion relation between the observed energy behaviors of the real and imaginary components of the optical potential. We have plotted the volume integrals per interacting nucleon pair of the best fit phenomenological potential, weighted by a Gaussian function $G(R)$ of the form

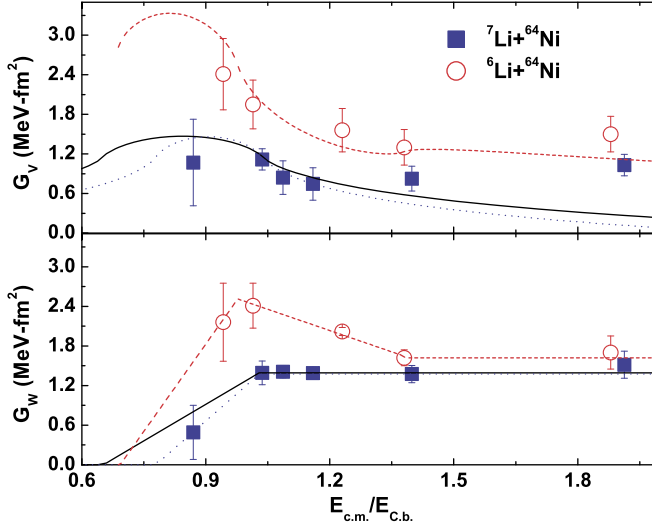$$G(R) = \frac{1}{\sqrt{2\pi}\sigma_G} exp\left[-\frac{(R - R_G)^2}{2\sigma_G^2}\right] \qquad (4)$$

Fig. 4. (Color online.) Gaussian weighted volume integrals of phenomenological real and imaginary potentials for ^{7}Li + ^{64}Ni system (solid square) and the same for ^{6}Li + ^{64}Ni with *hybrid* potential (open circle) from Ref. [15]. The solid and dotted curves represent the dispersion relation predictions for ^{7}Li + ^{64}Ni system [$E_{C.b.} = 12.44$ MeV, $R_G = 9.8$ fm and $\sigma_G = 0.4$ fm] using two different energies as *zero* absorption cross section, respectively, see text for details. The dashed curves indicate the same for ^{6}Li + ^{64}Ni system [$E_{C.b.} = 12.61$ MeV, $R_G = 9.8$ fm and $\sigma_G = 0.6$ fm] [15].

centered around an optimum radius R_G with a width of σ_G, as a function of incident energy. The volume integrals are, therefore, defined as

$$G_x(E) = \frac{4\pi}{A_P A_T} \int x(R, E) G(R) R^2 dR \qquad (5)$$

where x denotes either the real potential $V(R, E)$ or the imaginary potential $W(R, E)$ for the respective integral quantity. It was shown in Refs. [35,36] that the radial moments of the components of the complex optical potential satisfy the same dispersion relation that connects the real and the imaginary parts of the potential. For ^{7}Li + ^{64}Ni, R_G was chosen to be 9.8 fm, the value of R_M. The choice of σ_G was guided by the uncertainty associated with the estimated radius of sensitivity and it was taken to be 0.4 fm. The Gaussian weighted integral quantities, G_V(E) and G_W(E), with the real and the imaginary components of the phenomenological optical potential for ^{7}Li + ^{64}Ni system are plotted in Fig. 4 as a function of $E_{c.m.}/E_{C.b.}$. The error bars depict the dispersion in the integral values of the 'good' potentials at each energy, evaluated around the radius of R_G and with the width σ_G. Following Fig. 3, it is obvious that any of the chosen model potentials for ^{7}Li + ^{64}Ni system would give the same values for G_V and G_W within the error bars.

The curves in Fig. 4 depict the dispersion relation predictions. A simple two linear segments functional dependence of G_W(E) for ^{7}Li + ^{64}Ni in the dispersion integral predicts the corresponding energy dependence of G_V(E) shown in the figure. The dotted curve corresponds to the segment obtained by connecting the last two measured energy points for ^{7}Li + ^{64}Ni. The zero value of G_W, in this case, occurred at 10.8 MeV. The zero for the solid curve was determined, following Stelson et al. [37], from the extrapolation of linear dependence of the function $\sqrt{E}\sigma_r$ on E at low incident energies. The value of incident energy where G_W goes to zero for the latter choice was found to be 8.8 MeV. For both these cases, the predicted behavior of the real potential

exhibits the well known *bell shape* dependence in the energy region over which G_W goes to zero. But the peak of the bump occurred at lower energy beyond the Coulomb barrier energy. A sharp fall of the imaginary potential below the barrier yielded a narrower bump in the real potential and the behavior describes the extracted energy dependence (solid square) better in that energy domain though neither of them describe the data properly. The open circle and the dashed curve represent the energy dependence of Gaussian weighted volume integrals for the potential components and the corresponding predictions of dispersion relation for ^{6}Li + ^{64}Ni system taken from M. Biswas et al. [15]. In Ref. [15], gauss folding was performed with the *hybrid* model potential having folded real and phenomenological imaginary potential components. It is to be mentioned that with folded real potential, the G_V values obtained for ^{6}Li + ^{64}Ni are higher in magnitude than those obtained with phenomenological real potentials. With the empirical optical model potentials of Ref. [15], the resultant G_V values from gauss folding are close in magnitude, especially at above barrier energies, to those for ^{7}Li + ^{64}Ni system of the present study. As depicted in Fig. 2 of Ref. [15], the magnitudes of phenomenological real potential strength are lower in magnitude compared to the strengths of the folded real potential at the sensitive radius for all the measured energy values. However, the two model real potentials exhibit similar energy dependence. The ambiguity is not observed in the strengths of imaginary component the model potentials or the corresponding G_W values for ^{6}Li + ^{64}Ni. The comparison of the integral quantities, particularly the G_W values close to the barrier, therefore, indicates the influence of weaker binding of ^{6}Li over ^{7}Li in the energy variation of the effective potential for scattering with ^{64}Ni.

3.4. Radial distribution of absorption cross section

To gain further insight, the radial distribution of the total absorption cross section σ_r was computed as a function of radial separation, R of the colliding nuclei at each incident energy. If W(R) represents the imaginary component of the optical potential generating the absorption at a particular energy and $\chi_L(R)$ is the scattering wave function generated by the potential for partial wave L, total reaction cross section, σ_r, can be written as [38],

$$\sigma_r = \int_0^\infty \sigma_r(R)dR = \int_0^\infty \left[-\frac{8\pi}{\hbar k^2 v} W(R) \sum_L (2L+1)|\chi_L(R)|^2 \right] dR \qquad (6)$$

The radial absorption cross section $\sigma_r(R)$ is, therefore, defined by the integrand of the integral expression on the right hand side of Eq. (6). In the expression, k and v are the instantaneous momentum and relative velocity.

The radial distributions at each energy for ^{7}Li + ^{64}Ni system were generated with the best fit phenomenological potentials given in Table 1 and the plots are shown in Fig. 5 (a) and (c). The upper panel shows the distribution for the total absorptive potential while the lower panel shows the contributions of the volume and surface imaginary potentials separately. The peak of the surface absorption shifts to higher radius with lowering of the incident energy indicating absorption at large separation at lower energies. The feature corroborates the increasing *crossing radius* of total imaginary potential with decreasing energy. The peak of the distribution of absorption due to the volume term, describing the core fusion, does not shift which is expected as the volume imaginary component is fixed for all energies. However, it is to be noted that for ^{7}Li + ^{64}Ni system the two contributions dominating at different spatial regions are clearly separated. The

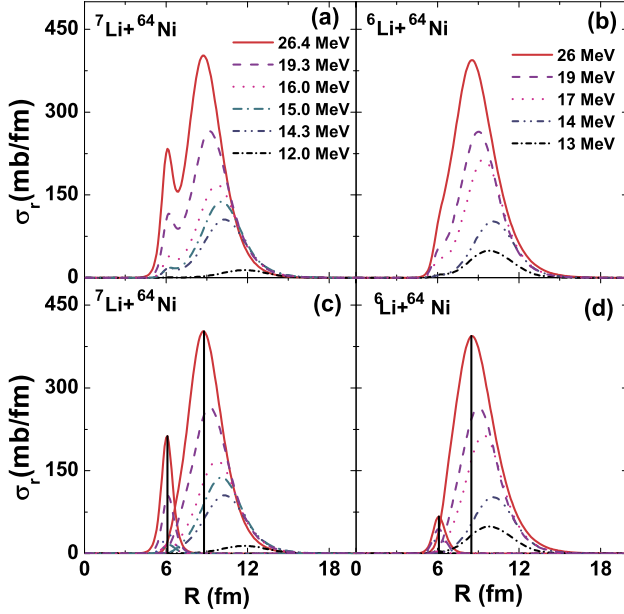Fig. 5. (Color online.) Radial distributions of absorption cross sections for ^{7}Li + ^{64}Ni [(a)&(c)] and for ^{6}Li + ^{64}Ni [(b)&(d)]. Radial distributions were generated with the phenomenological potentials. (a), (b) show the distributions of absorption for total imaginary and (c), (d) depict the contributions of volume (smaller peak on the left) and surface components of the imaginary potential separately at each energy. The solid lines in the lower panels indicate the locations of the sensitive radii at the highest energies of the respective systems.

Table 3
Comparison of components of absorption cross sections at equivalent center of mass energies for ^{6,7}Li + ^{64}Ni.

$E_{c.m.}$ (MeV)	^{7}Li + ^{64}Ni			^{6}Li + ^{64}Ni		
	σ_r (mb)	$\sigma_r{}^s$ (mb)	$\sigma_r{}^v$ (mb)	σ_r (mb)	$\sigma_r{}^s$ (mb)	$\sigma_r{}^v$ (mb)
23.8	1546.2	1314.7	231.5	1539.4	1460.1	79.3
17.4	1061.0	944.4	116.6	980.8	928.4	52.4
12.8	434.5	415.7	18.8	389.0	384.3	4.7

integrated values of the radial distributions of surface ($\sigma_r{}^s$) and volume ($\sigma_r{}^v$) absorptions are shown in Table 3 in comparison with the total absorption cross section.

4. Results and discussions

In the study of ^{7}Li + ^{64}Ni system, the primary motivation, as outlined in the introduction, is to look for the threshold behavior of the effective potential for ^{7}Li scattered from a medium mass target. The other aspect is to compare the observed behavior with that of ^{6}Li scattering from the same target. A distinction is expected because of higher breakup threshold and structural difference of ^{7}Li from ^{6}Li.

It is observed from Fig. 3, that both the phenomenological (variable and fixed geometry) potentials and the hybrid model potential fitting the angular distribution data equally well, ex-

hibit similar energy variations for the effective strength of the potentials for ^{7}Li + ^{64}Ni system. Within the error bars, the model potentials yield nearly the same strength around the sensitive radius. The surface strength of the imaginary potential remains almost independent of energy in above barrier region and it falls sharply below the barrier. The fall off of imaginary potential strength is guided by a single energy point below the barrier. With more number of energy points between the energy values of 14.3 MeV and 12 MeV, the lowest energy used, the fall of imaginary potential can be obtained with greater certainty. The energy variation is similar to the one observed for strongly bound systems, except that the fall off of imaginary potential with decreasing energy does not start before the Coulomb barrier energy is reached. This indicates the significant presence of open reaction channels even at energies comparable to the Coulomb barrier. Consequently, the effective real polarization contribution through dispersive correction gives an essence of TA like phenomenon with the *bell-shaped* peak being pushed to some lower energy beyond the threshold of Coulomb barrier *i.e.* the threshold pushed towards lower energies for ^{7}Li + ^{64}Ni system compared to strongly bound systems. Similar behavior of the interaction potential has been reported for this mass region in ^{7}Li + ^{59}Co [8] and in ^{7}Li + ^{80}Se [23]. The consistent picture evolving for this mass region differs from those observed for ^{7}Li scattering from heavier target masses. The energy dependence of the interaction potential near the barrier for ^{7}Li + ^{208}Pb [3] shows TA, like the strongly bound systems with the barrier as the threshold. But for ^{138}Ba [4] and ^{144}Sm [20] nuclei, the imaginary potential remains constant over the range of measured energies. The real potential for these systems exhibits a slow rise with decreasing energy. However, in a different analysis of the ^{7}Li + ^{138}Ba data, Lee et al. [39] observed that the imaginary potential strength in the above barrier region remains constant till the energy reaches the barrier and then falls sharply with energy decreasing below it. The energy dependence of the real potential for ^{7}Li + ^{138}Ba system, however, follows the shape of TA over the same energy domain. Thus the observation corroborates that for the mass region of the present study. On the other hand, for lighter mass targets the scenario is still more intriguing. In case of target nucleus ^{28}Si, the decreasing trend of the imaginary potential with decreasing energy on approaching the barrier is clearly visible but in the same energy domain the real potential also shows a decreasing trend. The observed behaviors of the real and imaginary potential are not connected by dispersion relation.

4.1. Comparison with ^{6}Li + ^{64}Ni

The comparative plots displaying the energy dependence of potentials for the projectiles ^{6}Li and ^{7}Li scattering from ^{64}Ni have been shown in Fig. 4. It is observed that the imaginary potential remains almost independent of energy for ^{7}Li projectile while for ^{6}Li it increases on approaching the barrier energy from above. Below the barrier, the imaginary potentials indicate a tendency to decrease although only one data point exits in the energy region both the systems. The difference in behavior is actually observed in the energy range around $E_{c.m.}/E_{C.b.} \sim 1.2$. While for ^{6}Li there is a rise in the imaginary strength, for ^{7}Li its independent of energy. The difference suggests the relative importance of reaction mechanisms other than fusion in absorbing flux from the entrance channel for these two projectiles when the incident energy approaches the barrier. With the threshold as low as 1.47 MeV, the break up of ^{6}Li projectile into two-body α–d clusters can be more dominant than the break up of ^{7}Li into α–t clusters (S$_\alpha$ = 2.47 MeV) in the same energy domain. On the other hand, in Ref. [40] it was shown that the energy dependence of the potential components near the threshold for ^{7}Li + ^{208}Pb is dominated by the coupling to one neutron transfer channel having a small negative Q-value. The channel (^{7}Li, ^{6}Li) also has a
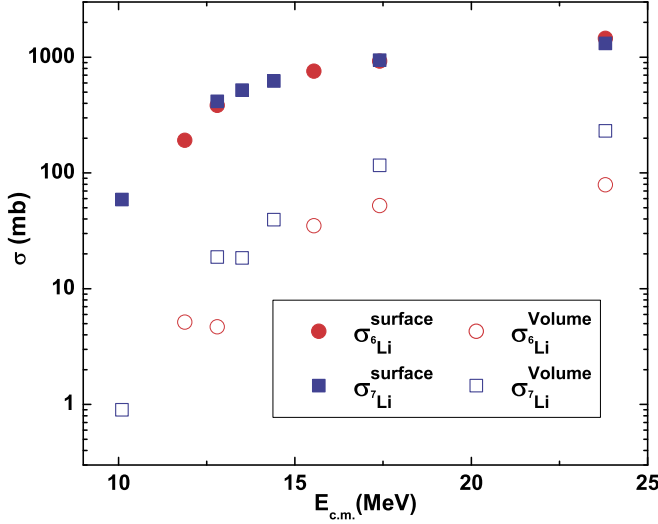
Fig. 6. (Color online.) Comparative plots of surface and volume absorption contributions of ^{7}Li (filled and open bullets) and ^{6}Li (filled and open squares). The filled symbols denote the surface and open symbols the volume absorption contributions respectively.

small negative Q-value for the target ^{64}Ni ($Q = -1.152$ MeV) and might have played a role in determining the nature of energy variation of the imaginary potentials around the barrier for the system ^{7}Li + ^{64}Ni. The one neutron transfer reaction (^{6}Li, ^{5}Li) with the ^{64}Ni target has a Q-value of $+0.434$ MeV producing a three-body final state of α, p and ^{65}Ni. Significant presence of this channel can also induce an energy dependence observed for the imaginary potential for ^{6}Li + ^{64}Ni. The polarization contribution to the real optical potential from the energy dependence of the imaginary component pushed the peaks towards lower energies beyond the Coulomb barrier energy for both the projectiles though the shift is more and the rise is sharper for ^{6}Li. Also a careful look at Fig. 4, shows that for ^{6}Li there is an indication of a broad dip around $E_{c.m.}/E_{C.b.} \sim 1.2$ in the energy dependence of real potential. The behavior of real potential in ^{6}Li coincides with a corresponding rise in the imaginary potential strength. This particular behavior is absent for ^{7}Li projectile, which on the other hand, presents an energy variation more like a strongly bound projectile.

Besides comparing the nature of energy dependence of the potential, an interesting feature also comes out from the comparison of the variation of absorption cross section as a function of radial separation of the colliding nuclei shown in Fig. 5. The core fusion contribution, coming from the energy independent volume imaginary potential W_F, is more for ^{7}Li than ^{6}Li at each energy. This implies that the incident wave does not reach the radius of $R_F = 1.0 \times (A_P^{\frac{1}{3}} + A_T^{\frac{1}{3}})$ with sufficient intensity after the absorption at the surface, to produce the core fusion with the target for ^{6}Li compared to ^{7}Li projectile. It is obvious from Table 3 that at similar incident energy the core fusion component is more than a factor of two smaller for ^{6}Li though the surface absorption component is comparable to that of ^{7}Li, especially at higher energy regime.

Apart from having a larger volume absorption over the entire measured energy range, the projectile ^{7}Li apparently has larger absorption at the surface at energies below the barrier as is seen from Fig. 6. This particular feature is opposite to that observed for high Z targets like ^{208}Pb [3], where the absorption cross section is more for ^{6}Li compared to ^{7}Li around the barrier

energies. This indicates the presence of a reaction channel other than the breakup of ^{7}Li at these low energies for lower mass targets. On the other hand, for high Z heavy targets like ^{208}Pb [3], Coulomb induced breakup of ^{6}Li compared to ^{7}Li is more dominant direct reaction around the barrier energies producing larger absorption cross section but for low Z targets this contribution is significantly reduced. Hence a relative change in the reaction mechanisms with decreasing mass and incident energy for the two projectiles is responsible for the difference in the total absorption cross sections. It will be extremely interesting to compare the fusion excitation function for ^{6,7}Li on ^{64}Ni at sub-barrier energies to identify the effect of this process on fusion.

5. Summary

To summarize, the measurement of elastic angular distributions for the system ^{7}Li + ^{64}Ni at energies around the barrier in the range of 12 MeV $\leq E_{lab} \leq$ 26.4 MeV had been performed. Optical model analyses of the measured data were done using three different model potentials. The energy dependence of the components of the effective potentials was subsequently extracted.

It has been found that for the system ^{7}Li + ^{64}Ni the threshold behavior of the effective potential describing the elastic scattering is more like a tightly bound system but with the *threshold* set at a lower energy than the Coulomb barrier. With decreasing energy the imaginary potential strength remains invariant till the barrier is reached. This behavior is in contrast to the observation for the system ^{6}Li + ^{64}Ni. Consequently the rise in the real potential strength is also shifted to energies below the barrier, *i.e.* the threshold is shifted to lower energy.

A comparison of the nature of absorption as a function of radial separation with the target for the two Li isotopes has also been done. Observations indicate that ^{7}Li has higher core fusion component at all energies. However, the contribution of surface absorption between the two isotopes changes with decreasing bombarding energy. It is observed from Table 3 that, at the measured highest incident energy the surface contribution for ^{6}Li, with lower break up threshold, is more than ^{7}Li. On the other hand at the measured lowest incident energy below the barrier, the surface absorption of ^{7}Li is more than ^{6}Li. This aspect needs to be probed further with accurate measurement of elastic angular distribution at smaller energy steps around the barrier.

Acknowledgements

References

[1] L.F. Canto, P.R.S. Gomes, R. Donangelo, M.S. Hussein, Phys. Rep. 424 (2006) 1.
[2] M. Dasgupta, D.J. Hinde, N. Rowley, A.M. Stefanini, Annu. Rev. Nucl. Part. Sci. 48 (1998) 401.
[3] N. Keeley, S.J. Bennett, N.M. Clarke, B.R. Fulton, G. Tungate, P.V. Drumm, M.A. Nagarajan, J.S. Lilley, Nucl. Phys. A 571 (1994) 326.
[4] A.M.M. Maciel, P.R.S. Gomes, J. Lubian, R.M. Anjos, R. Cabezas, G.M. Santos, C. Muri, S.B. Moraes, R.L. Neto, N. Added, N.C. Filho, C. Tenreiro, Phys. Rev. C 59 (1999) 2103.
[5] M.A. Tiede, D.E. Trcka, K.W. Kemper, Phys. Rev. C 44 (1991) 1698.

[6] A. Pakou, N. Alamanos, G. Doukelis, A. Gillibert, G. Kalyva, M. Kokkoris, S. Kossionides, A. Lagoyannis, A. Musumarra, C. Papachristodoulou, N. Patronis, G. Perdikakis, D. Pierroutsakou, E.C. Pollacco, K. Rusek, Phys. Rev. C 69 (2004) 054602;
   A. Pakou, K. Rusek, Phys. Rev. C 69 (2004) 057602.
[7] J.M. Figueira, J.O. Fernández Niello, D. Abriola, A. Arazi, O.A. Capurro, E. de Barbara, G.V. Martí, D. Martínez Heimann, A.E. Negri, A.J. Pacheco, I. Padron, P.R.S. Gomes, J. Lubian, T. Correa, B. Paes, Phys. Rev. C 75 (2007) 017602.
[8] F.A. Souza, L.A.S. Leal, N. Carlin, M.G. Munhoz, R. Liguori Neto, M.M. de Moura, A.A.P. Suaide, E.M. Szanto, A. Szanto de Toledo, J. Takahashi, Phys. Rev. C 75 (2007) 044601.
[9] D.J. Hinde, M. Dasgupta, B.R. Fulton, C.R. Morton, R.J. Wooliscroft, A.C. Berriman, K. Hagino, Phys. Rev. Lett. 89 (2002) 272701.
[10] E.F. Aguilera, J.J. Kolata, F.D. Becchetti, P.A. DeYoung, J.D. Hinnefeld, A. Horvath, L.O. Lamm, Hye-Young Lee, D. Lizcano, E. Martínez-Quiroz, P. Mohr, T.W. O'Donnell, D.A. Roberts, G. Rogachev, Phys. Rev. C 63 (2001) 061603(R).
[11] P.R.S. Gomes, I. Padron, M.D. Rodríguez, G.V. Martí, R.M. Anjos, J. Lubian, R. Veiga, R. Liguori Neto, E. Crema, N. Added, L.C. Chamon, J.O. Fernández Niello, O.A. Capurro, A.J. Pacheco, J.E. Testoni, D. Abriola, A. Arazi, M. Ramírez, M.S. Hussein, Phys. Lett. B 601 (2004) 20.
[12] R.S. Mackintosh, A.M. Kobos, Phys. Lett. B 116 (1982) 95.
[13] Y. Sakuragi, M. Yahiro, M. Kamimura, Prog. Theor. Phys. Suppl. 89 (1986) 189.
[14] G.R. Satchler, Phys. Rep. 199 (1991) 147.
[15] M. Biswas, Subinit Roy, M. Sinha, M.K. Pradhan, A. Mukherjee, P. Basu, H. Majumdar, K. Ramachandran, A. Shrivastava, Nucl. Phys. A 802 (2008) 67.
[16] A. Di Pietro, J. Phys. Conf. Ser. 205 (2010) 012042.
[17] N.N. Deshmukh, S. Mukherjee, D. Patel, N.L. Singh, P.K. Rath, B.K. Nayak, D.C. Biswas, S. Santra, E.T. Mirgule, L.S. Danu, Y.K. Gupta, A. Saxena, R.K. Choudhury, R. Kumar, J. Lubian, C.C. Lopes, E.N. Cardozo, P.R.S. Gomes, Phys. Rev. C 83 (2011) 024607.
[18] M.S. Hussein, P.R.S. Gomes, J. Lubian, L.C. Chamon, Phys. Rev. C 73 (2006) 044610.
[19] N. Keeley, K. Rusek, Phys. Lett. B 427 (1998) 1.
[20] J.M. Figueira, J.O. Fernandez Niello, A. Arazi, O.A. Capurro, P. Carnelli, L. Fimiani, G.V. Martí, D. Martinez Heimann, A.E. Negri, A.J. Pacheco, J. Lubian, D.S. Monteiro, P.R.S. Gomes, Phys. Rev. C 81 (2010) 024613.
[21] P.R.S. Gomes, I. Padron, J.O. Fernández Niello, G.V. Martí, M.D. Rodríguez, O.A. Capurro, A.J. Pacheco, J.E. Testoni, A. Arazi, J. Lubian, R.M. Anjos, L.C. Chamon, E. Crema, M.S. Hussein, J. Phys. G, Nucl. Phys. 31 (2005) S1669.
[22] N.N. Deshmukh, S. Mukherjee, B.K. Nayak, D.C. Biswas, S. Santra, E.T. Mirgule, S. Appannababu, D. Patel, A. Saxena, R.K. Choudhury, J. Lubian, P.R.S. Gomes, Eur. Phys. J. A 47 (2011) 118.
[23] L. Fimiani, J.M. Figueira, G.V. Martí, J.E. Testoni, A.J. Pacheco, W.H.Z. Cárdenas, A. Arazi, O.A. Capurro, M.A. Cardona, P. Carnelli, E. de Barbará, D. Hojman, D. Martinez Heimann, A.E. Negri, Phys. Rev. C 86 (2012) 044607.
[24] C. Beck, N. Keeley, A. Diaz-Torres, Phys. Rev. C 75 (2007) 054605.
[25] J.M. Figueira, D. Abriola, J.O. Fernández Niello, A. Arazi, O.A. Capurro, E. de Barbara, G.V. Martí, D. Martínez Heimann, A.J. Pacheco, J.E. Testoni, I. Padron, P.R.S. Gomes, J. Lubian, Phys. Rev. C 73 (2006) 054603.
[26] Computer code LAMPS (Linux Advanced Multiparameter System), www.tifr.res.in/~pell/lamps.html.
[27] I.J. Thompson, SFRESCO, search version of code FRESCO(v2.9), Comput. Phys. Rep. 7 (1988) 167.
[28] G.R. Satchler, W.G. Love, Phys. Rep. 55 (1979) 183.
[29] Dao T. Khoa, W. von Oertzen, Phys. Lett. B 304 (1993) 8;
   Dao T. Khoa, W. von Oertzen, H.G. Bohlen, Phys. Rev. C 49 (1994) 1652.
[30] A.M. Kobos, B.A. Brown, P.E. Hodgson, G.R. Satchler, A. Budzanowski, Nucl. Phys. A 384 (1982) 65.
[31] http://www-nds.iaea.org/ripl-2.
[32] H. De Vries, C.W. Jager, C. De Vries, At. Data Nucl. Data Tables 36 (1987) 495.
[33] Mili Biswas, Phys. Rev. C 77 (2008) 017602.
[34] M.E. Brandan, J.R. Alfaro, A. Menchaca-Rocha, J. Gomez del Campo, G.R. Satchler, P.H. Stelson, H.J. Kim, D. Shapira, Phys. Rev. C 48 (1993) 1147.
[35] C. Mahaux, H. Ngo, G.R. Satchler, Nucl. Phys. A 449 (1986) 354.
[36] C. Mahaux, H. Ngo, G.R. Satchler, Nucl. Phys. A 456 (1986) 134.
[37] P.H. Stelson, Phys. Lett. B 205 (1988) 190;
   P.H. Stelson, H.J. Kim, M. Beckerman, D. Shapira, R.L. Robinson, Phys. Rev. C 41 (1990) 1584.

[38] J.C. Pacheco, B. Bilwes, F. Sanchez, J.A. Ruiz, J. Diaz, J.L. Ferrero, M.D. Kadi-Hanifi, Nucl. Phys. A 588 (1995) 537;
J.C. Pacheco, M.D. Kadi-Hanifi, B. Bilwes, F. Remiro, Phys. Rev. C 59 (1999) 1518.
[39] Su Youn Lee, Myung Ki Cheoun, Woonyoung So, Eunja Ha, Kyungsik Kim, J. Korean Phys. Soc. 55 (2009) 2123.
[40] N. Keeley, K. Rusek, Phys. Rev. C 56 (1997) 3421.